Research Article | Vol. 25, No. 17 | 21 Aug 2017 | OPTICS EXPRESS 20663
Optics EXPRESS

1.5 μm polarization coherent lidar incorporating time-division multiplexing

CHONG WANG,[1] HAIYUN XIA,[1,*] MINGJIA SHANGGUAN,[1] YUNBIN WU,[1] LU WANG,[1] LIJIE ZHAO,[1] JIAWEI QIU,[1] AND RENJUN ZHANG[2]

[1]*CAS Key Laboratory of Geospace Environment, USTC, Hefei, 230026, China*
[2]*Honglulin Lidar Science and technology CO. LTD, Nanjing, 211000, China*
**hsia@ustc.edu.cn*

Abstract: Atmospheric depolarization ratio and wind velocity are measured simultaneously by a single versatile coherent Doppler lidar (CDL). Backscattering components at parallel and perpendicular polarization states are obtained by using a single balanced detector, adopting time-division multiplexing technique. Thus systematic error induced by the non-uniform response of different detectors in traditional lidars is avoided. The operation mode of the instrument can be switched from polarization CDL to traditional CDL by the user depending on atmospheric conditions and desired performance. As demonstrated, the perpendicular component of the backscattering, usually wasted, not only can be used to retrieve the ADR, but also can be used to improve the carrier to noise ratio in wind detection. In the traditional mode, given a tolerance of 0.5 m/s precision, a detection range of 6 km is achieved by using a 300 ns laser pulse with energy of 100 μJ, where the temporal and spatial resolution of 2 s and 60 m, respectively. Continuous wind detection of the atmospheric boundary layer over 26 hours is presented to demonstrate the robustness and stability of the system. Dynamic evolution and wind structure are recorded.

© 2017 Optical Society of America

OCIS codes: (010.0010) Atmospheric and oceanic optics; (280.0280) Remote sensing and sensors; (010.3640) Lidar; (280.3340) Laser Doppler velocimetry; (040.2840) Heterodyne.

References and links

1. G. Fiocco and L. D. Smullin, "Detection of scattering layers in the upper atmosphere (60-140 km) by optical radar," Nature **199**(4900), 1275–1276 (1963).
2. M. Shangguan, H. Xia, C. Wang, J. Qiu, G. Shentu, Q. Zhang, X. Dou, and J. W. Pan, "All-fiber upconversion high spectral resolution wind lidar using a Fabry-Perot interferometer," Opt. Express **24**(17), 19322–19336 (2016).
3. H. Xia, X. Dou, D. Sun, Z. Shu, X. Xue, Y. Han, D. Hu, Y. Han, and T. Cheng, "Mid-altitude wind measurements with mobile Rayleigh Doppler lidar incorporating system-level optical frequency control method," Opt. Express **20**(14), 15286–15300 (2012).
4. X. H. Xue, X. K. Dou, J. Lei, J. S. Chen, Z. H. Ding, T. Li, Q. Gao, W. W. Tang, X. W. Cheng, and K. Wei, "Lower thermospheric-enhanced sodium layers observed at low latitude and possible formation: case studies," J. Geophys. Res. **118**(5), 2409–2418 (2013).
5. H. Xia, G. Shentu, M. Shangguan, X. Xia, X. Jia, C. Wang, J. Zhang, J. S. Pelc, M. M. Fejer, Q. Zhang, X. Dou, and J. W. Pan, "Long-range micro-pulse aerosol lidar at 1.5 μm with an upconversion single-photon detector," Opt. Lett. **40**(7), 1579–1582 (2015).
6. C. Wu, F .Yi, "Local ice formation via liquid water growth in slowly-ascending humid aerosol/liquid water layers observed with ground-based lidars and radiosondes," J. Geophys. Res. (in press, 2017).
7. J. Shaw, N. Seldomridge, D. Dunkle, P. Nugent, L. Spangler, J. Bromenshenk, C. Henderson, J. Churnside, and J. Wilson, "Polarization lidar measurements of honey bees in flight for locating land mines," Opt. Express **13**(15), 5853–5863 (2005).
8. J. H. Churnside, J. J. Wilson, and V. V. Tatarskii, "Airborne lidar for fisheries applications," Opt. Eng. **40**(3), 406–414 (2001).
9. T. Fujii and T. Fukuchi, *Laser Remote Sensing* (Boca Raton, Taylor & Francis, 2005), Chap. 7.
10. W. Diao, X. Zhang, J. Liu, X. Zhu, Y. Liu, D. Bi, and W. Chen, "All fiber pulsed coherent lidar development for wind profiles measurements in boundary layers," Chin. Opt. Lett. **12**(7), 072801 (2014).
11. A. D. Bouteyre, G. Canat, M. Valla, B. Augère, C. Besson, D. Goular, L. Lombard, J.-P. Cariou, A. Durecu, D. Fleury, L. Bricteux, S. Brousmiche, S. Lugan, and B. Macq, "Pulsed 1.5ìm lidar for axial aircraft wake vortex detection based on high brightness large-core fiber amplifier," IEEE J. Sel. Top. Quantum Electron. **15**(2), 441–450 (2009).

#296321 https://doi.org/10.1364/OE.25.020663
Journal © 2017 Received 18 May 2017; revised 28 Jul 2017; accepted 14 Aug 2017; published 16 Aug 2017

Optics EXPRESS

12. G. J. Koch, J. Y. Beyon, B. W. Barnes, M. Petros, J. Yu, F. Amzajerdian, M. J. Kavaya, and U. N. Singh, "High-energy 2 μm doppler lidar for wind measurements," Opt. Eng. **46**, 116201 (2007).
13. S. C. Tucker, C. J. Senff, A. M. Weickmann, W. A. Brewer, R. M. Banta, S. P. Sandberg, D. C. Law, and R. M. Hardesty, "Doppler lidar estimation of mixing height using turbulence, shear and aerosol profiles," J. Atmos. Ocean. Technol. **26**(4), 673–688 (2009).
14. M. Kavaya, J. Beyon, G. Koch, M. Petros, P. Petzar, U. Singh, B. Trieu, and J. Yu, "The Doppler aerosol wind (DAWN) airborne, wind-profiling, coherent-detection lidar system: overview and preliminary flight results," J. Atmos. Ocean. Technol. **31**(4), 826–842 (2014).
15. R. M. Huffaker and R. M. Hardesty, "Remote sensing of atmospheric wind velocities using solid-state and CO2 coherent laser systems," Proc. IEEE **84**(2), 181–204 (1996).
16. F. Chouza, O. Reitebuch, S. Groß, S. Rahm, V. Freudenthaler, C. Toledano, and B. Weinzierl, "Retrieval of aerosol backscatter and extinction from airborne coherent Doppler wind lidar measurements Atmos," Meas. Tech. **8**(7), 2909–2926 (2015).
17. J. Kuttippurath, F. Lefevre, J. Pommereau, H. Roscoe, F. Goutail, A. Pazmino, and J. Shanklin, "NDACC/SAOZ UV-visible total ozone measurements: improved retrieval and comparison with correlative ground-based and satellite observations," Atmos. Chem. Phys. **11**(12), 5975–5995 (2011).
18. A. Ansmann, M. Tesche, P. Seifert, S. Groß, V. Freudenthaler, A. Apituley, K. M. Wilson, I. Serikov, H. Linné, B. Heinold, A. Hiebsch, F. Schnell, J. Schmidt, I. Mattis, U. Wandinger, and M. Wiegner, "Ash and fine-mode particle mass profiles from EARLINET-AERONET observations over central Europe after the eruptions of the Eyjafjallajökull volcano in 2010," J. Geophys. Res. **116**, D00U02 (2011).
19. T. Murayama, N. Sugimoto, I. Uno, K. Kinoshita, K. Aoki, N. Hagiwara, Z. Liu, I. Matsui, T. Sakai, T. Shibata, K. Arao, B.-J. Sohn, J.-G. Won, S.-C. Yoon, T. Li, J. Zhou, H. Hu, M. Abo, K. Iokibe, R. Koga, and Y. Iwasaka, "Ground-based network observation of Asian dust events of April 1988 in east Asia," J. Geophys. Res. **106**(D16), 18345–18359 (2001).
20. D. Althausen, R. Engelmann, H. Baars, B. Heese, A. Ansmann, D. Müller, and M. Komppula, "Portable Raman lidar PollyXT for automated profiling of aerosol backscatter, extinction, and depolarization," J. Atmos. Ocean. Technol. **26**(11), 2366–2378 (2009).
21. D. M. Winker, M. A. Vaughan, A. Omar, Y. Hu, K. A. Powell, Z. Liu, W. H. Hunt, and S. A. Young, "Overview of the CALIPSO Mission and CALIOP data processing algorithms," J. Atmos. Ocean. Technol. **26**(11), 2310–2323 (2009).
22. S. D. Mayor, S. M. Spuler, B. M. Morley, and E. Loew, "Polarization lidar at 1.54μm and observations of plumes from aerosol generators," Opt. Eng. **46**, 096201 (2007).
23. P. Dérian, C. F. Mauzey, and S. D. Mayor, "Wavelet-based optical flow for two-component wind field estimation from single aerosol lidar data," J. Atmos. Ocean. Technol. **32**(10), 1759–1778 (2015).
24. S. D.Mayor, A. Petrova-Mayor, B. Morley, and S. Spuler, "Recent improvements to the Raman-shifted eye-safe aerosol lidar (REAL)," Proc. SPIE **9972**, 997210 (2013).
25. C. F. Abari, X. Chu, R. Michael Hardesty, and J. Mann, "A reconfigurable all-fiber polarization-diversity coherent Doppler lidar: principles and numerical simulations," Appl. Opt. **54**(30), 8999–9009 (2015).
26. J. F. Holmes and B. J. Rask, "Optimum optical local-oscillator power levels for coherent detection with photodiodes," Appl. Opt. **34**(6), 927–933 (1995).
27. M. Shangguan, C. Wang, H. Xia, G. Shentu, X. Dou, Q. Zhang, and J. Pan, "Brillouin optical time domain reflectometry for fast detection of dynamic strain incorporating double-edge technique," Opt. Commun. **398**, 95–100 (2017).
28. K. Sassen, "The polarization lidar technique for cloud research: a review and current assessment," Bull. Am. Meteorol. Soc. **72**(12), 1848–1866 (1991).
29. Z. Wang, R. Chi, B. Liu, and J. Zhou, "Depolarization properties of cirrus clouds from polarization lidar measurements over Hefei in spring," Chin. Opt. Lett. **6**(4), 235–237 (2008).
30. T. Murayama, H. Okamoto, N. Kaneyasu, H. Kamataki, and K. Miura, "Application of lidar depolarization measurement in the atmospheric boundary layer: Effects of dust and sea-salt particles," J. Geophys. Res. **104**(24), 31781 (1999).
31. T. Sakaï, T. Nagai, Y. Zaizen, and Y. Mano, "Backscattering linear depolarization ratio measurements of mineral, sea-salt, and ammonium sulfate particles simulated in a laboratory chamber," Appl. Opt. **49**(23), 4441–4449 (2010).
32. G. David, B. Thomas, T. Nousiainen, A. Miffre, and P. Rairoux, "Retrieving simulated volcanic, desert dust, and sea-salt particle properties from two / three-component particle mixtures using UV-VIS polarization Lidar and T-matrix," Atmos. Chem. Phys. **13**(14), 6757–6776 (2013).
33. A. Dolfi-Bouteyre, B. Augere, M. Valla, D. Goular, D. Fleury, G. Canat, C. Planchat, T. Gaudo, C. Besson, A. Gilliot, J.-P. Cariou, O. Petilon, J. Lawson-Daku, S. Brousmiche, S. Lugan, L. Bricteux, and B. Macq, "Aircraft wake vortex study and characterization with 1.5 μm fiber Doppler lidar," Aerosp. Lab. **1**, 1 (2009).
34. L. Bricteux, Simulation of turbulent aircraft wake vortex flows and their impact on the signals returned by a coherent Doppler LIDAR system," PhD thesis, Université catholique de Louvain (2008).
35. J. Mann, J. P. Cariou, M. Courtney, P. Parmentier, T. Mikkelsen, R. Wagner, P. J. P. Lindelöw, M. Sjöholm, and K. Enevoldsen, "Comparison of 3D turbulence measurements using three staring wind lidars and a sonic anemometer," Meteorol. Z. **18**(2), 135–140 (2009).

Optics EXPRESS

36. R. G. Frehlich, S. M. Hannon, and S. W. Henderson, "Performance of a 2-μm coherent Doppler lidar for wind measurements," J. Atmos. Ocean. Technol. **11**(6), 1517–1528 (1994).
37. B. J. Rye and R. M. Hardesty, "Discrete spectral peak estimation in incoherent backscatter heterodyne lidar. I: Spectral accumulation and the Cramer-Rao lower bound," IEEE Trans. Geosci. Remote Sens. **31**(1), 16–27 (1993).
38. B. J. Rye and R. M. Hardesty, "Discrete spectral peak estimation in incoherent backscatter heterodyne lidar. II. Correlogram accumulation," IEEE Trans. Geosci. Remote Sens. **31**(1), 28–35 (1993).

1. Introduction

In 1963, Fiocco and Smullin demonstrated one of the earliest applications of lidar for atmospheric characterizations and meteorological observations [1]. After five decades of development and modification, lidar systems matured and became sophisticated, allowing detection of a rich variety of atmospheric parameters on a rounine basis. In this work, two different detection schemes are integrated into a unique simplified all-fiber system. Doppler lidars can measure wind velocity from the atmospheric boundery layer to the thermosphere via backscatterings from aerosol [2], molecules [3] and metallic species [4] including resonance fluorescence. Polarization lidars have been widely used in many applications, such as monitoring of air pollution [5], classification of cloud [6] and aerosol phase [22], searching for swarms of bees [7] or schools of fish [8].

There are two fundamental methods used in Doppler lidar, direct detection lidar (DDL) and coherent detection lidar (CDL). DDL uses an optical frequency discriminator or spectrum analyzer to convert the Doppler shift into power fluctuation or optical pattern change. CDL uses a local oscillator mixed with the atmospheric backscattering, resulting in an RF beating signal. After Fourier transformation (FT), the Doppler shift caused by wind in the line-of-sight of the lidar can be retrieved. A key feature of the CDL is that the backscattering gets "amplified" by the local oscillator. For a well-designed CDL, in principle, its detectivity can approach the quantum limit [9]. Thanks to these merits, CDL has been used on ground-based [10–12], ship-based [13, 14] and airborne [15, 16] platforms.

In atmospheric monitoring, there are many continuous observations from polarization lidar systems in the world, such as Network for the Detection of Atmospheric Composition Change (NDACC) [17], European Aerosol Research Lidar Network (EARLINET) [18], Asian Dust and Aerosol Lidar Observation Networks (AD-Net) [19], Global Atmosphere Watch (GAW) Aerosol Lidar Observation Network (GALION) [20], and Cloud-aerosol Lidar And Infrared Pathfinder Satellite Observations (CALIPSO) [21].

Simultaneous detection of the wind velocity and the atmospheric depolarization ratio (ADR) have been reported using Mie scattering lidars [22–24]. Despite the popularization of Doppler lidar and polarization lidar, there does not yet appear to be a single CDL that can achieve this goal. A principle simulation has been reported [25]. However, four balanced detectors were used, making the system complicated, expensive and unstable in practical routine operation. Since the non-uniform response of the detectors will induce systematic errors, frequent calibration should be performed in the traditional polarization lidars.

In this paper, an all-fiber polarization coherent Doppler lidar is demonstrated for simultaneous detection of atmospheric wind and depolarization ratio. Using time-division multiplexing (TDM) technique, only one balanced detector is used to detect the two backscattering components in orthogonal polarization states, making the system stable and calibration-free. As we demonstrated later, both the backscattering components in parallel and perpendicular polarization states can be used to retrieve the wind profiles, which will improve the detection accuracy if the ADR is high. According to the optical terminology, the parallel and perpendicular polarization states are abbreviated as P and S in this paper, respectively.

The remainder of the paper is organized as follows. In Section 2, the principle and instrument are introduced. In Section 3, simultaneous detection of wind velocity and ADR is performed. Finally, analysis of the results is carried out.

Optics EXPRESS

2. Principle and Instrument

Due to the depolarization effect of atmospheric aerosol, the polarization state of the backscattering will change from that of the original outgoing laser pulse. Generally, the CDL can't measure the depolarization ratio of the atmosphere since only the backscattering component parallel to the polarization plane of the transmitted laser beam is detected. The other backscattering component in perpendicular state is wasted. To resolve this problem, a compact and versatile optical layout is built using a TDM technique, as shown in Fig. 1. The DFB master laser emits a CW waveform at P state, the polarization-maintaining beam splitter divides the laser into local oscillator and transmitted laser beam. The power of the local oscillator is tuned to be 1 mW [26] by a tunable attenuator. The continuous laser is chopped into a pulse train by using an acousto-optical modulator (AOM). A frequency shift of 80 MHz is carried in the 300 ns laser pulse. After going through an erbium doped fiber amplifier (EDFA), the pulse energy is amplified to 100 μJ and then collimated and directed to the atmosphere. The backscattering is received by using a coupler and then divided into P and S polarization channels according to the orthogonal polarization states by using a polarization beam splitter (PBS). The P state backscattering is sent into a 3-km polarization maintaining fiber (PMF), which is used as a delay line; and the S state backscattering is converted to P state by changing the panda fiber's axis, which has been integrated in the PBS, an adapter is illustrated in Fig. 1 for easily understand. An optical switch (OS) is used to select the signal sent to the 3-dB coupler in the time sequence. Since the extinction ratio of the OS is as low as −35dB, the cross-talk between backscattering at two orthogonal states is negligible. Finally, the selected backscattering is mixed with the local oscillator and measured by a balanced detector (BD). Here, the PBS, the PMF delayer and the OS form a TDM module, making it possible to detect the ADR with a single balanced detector.

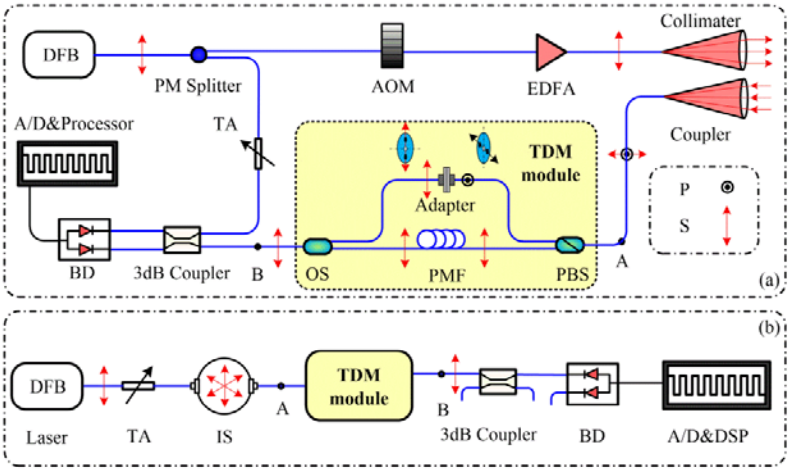

Fig. 1. (a). Optical layout of the versatile coherent Doppler lidar incorporating time division multiplexing. DFB, distributed feedback diode; PM Splitter, polarization-maintaining beam splitter; TA, tunable attenuator; AOM, acousto-optic modulator; EDFA, erbium doped fiber amplifier; PBS, polarization beam splitter; PMF, polarization maintaining fiber; OS, optical switch; BD, balanced detector; Fig. 1(b). Optical layout of calibration; IS, integrating sphere.

The digital signal processor (DSP) card in the computer will perform the fast FT to the RF signal from the A/D converter and export the power spectrum to CPU. Then, the Doppler frequency shift is retrieved using a maximum likelihood discrete spectral (MLDSP) algorithm, and the ADR is calculated with the carrier to noise ratio (CNR).

This depolarization CDL can be operated in two modes: depolarization mode and traditional mode. If only the wind velocity is needed, depolarization mode can be easily

Optics EXPRESS

switched to traditional mode by connecting point A and point B in Fig. 1. Note that, the TDM technique can only be used at optical communication band, particularly at working wavelength of 1.5 μm, due to its lowest attenuation (<1 dB/km) in the fiber [27]. Figure 2 is a photograph of one pair of the CDLs sharing one set of computer. The main specifications and manufacturers of the lidar system are listed in Table 1.

Fig. 2. Photograph of one pair of CDLs sharing one set of computer.

Table 1. The main specifications and manufacturers of lidar system components

	Parameter	Value	Manufacturer
Laser	Wavelength (nm)	1548.1	Keopsys (France)
	Pulse energy (μJ)	100	
	Pulse duration (ns)	300	
	Pulse rate (Hz)	15625	
	Local oscillator power (mW)	1	
	AOM (MHz)	80	
Telescope	Diameter (mm)	80	Honglulin (China)
Detector	BD bandwidth (MHz)	200	Thorlabs (USA)
ADC	ADC rate (MHz)	250	Spectrum(Germany)
DSP	TMS320C6678		Texas Instruments (USA)

In order to obtain the ADR, the ratio of insertion losses at the two orthogonal states should be calibrated at the initialization of the system. Figure 1(b) shows the optical layout for the calibration procedure. The DFB laser is fed to an integrating sphere, in which the polarization state is spread in all directions evenly. The output light from the integrating sphere is connected with the TDM module. By measuring the power ratio of signals at two polarization channels in the TDM setup, the ratio of insertion losses can be determined. Because this CDL uses all-fiber and a polarization maintaining optical layout, the impacts of circumstance disturbances, such as vibrations and temperature changes, are neglected.

The detection range of the depolarized channel d is simply decided by the length of the PMF,

$$d = \frac{l \cdot n_f}{2n_a}, \tag{1}$$

where l is the length of the PMF, n_f and n_a are the refractive indexes of the PMF and the air. In this work, given $l = 3$ km and $n_f / n_a = 1.4685$, d is calculated to be 2202.75 m.

For the reader's convenience, the time sequence of the instrument is illustrated, in Fig. 3. Usually, the ADR is lower than 0.1. So the backscattering at the S state is detected firstly. Thanks to the ultralow attenuation loss at 1.5 μm, the backscattering at the P state is delayed by using a 3-km PMF, according to the Eq. (1), and a corresponding time delay of 15 μs. Finally, both the signals at the two orthogonal states are selected alternatively and combined with the OS. By using TDM technique, the polarization CDL is simplified. And, the

Optics EXPRESS

backscattering at two orthogonal states certainly comes from the same atmospheric aerosol particles.

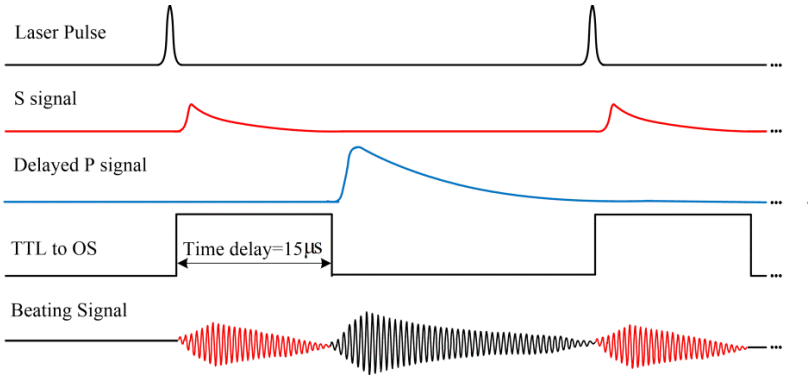

Fig. 3. Timing sequence of time-division multiplexing in the experiments. The TTL is set to a high level when the laser pulse is emitted immediately, the S state signal is detected with a duration of 15μs. Then, the TTL is set to a low level and the delayed P state signal is detected until next laser pulse.

The lidar equations of the polarization lidar at two polarization states are defined as

$$N_{\parallel}(R)=E_0\frac{\eta_q}{h\nu}\frac{A_0}{R^2}\xi(R)\beta_{\parallel}(R)k_{\parallel}\exp\left[-2\int_0^R\sigma_{\parallel}(r)dr\right], \tag{2}$$

$$N_{\perp}(R)=E_0\frac{\eta_q}{h\nu}\frac{A_0}{R^2}\xi(R)\beta_{\perp}(R)k_{\perp}\exp\left[-\int_0^R\sigma_{\parallel}(r)+\sigma_{\perp}(r)dr\right], \tag{3}$$

where E_0 is the laser energy, η_q is the quantum efficiency, h is the Plank constant, υ is the laser central frequency, A_0 is the area of the telescope, R is the distance to the telescope, $\xi(R)$ is the geometrical overlap factor at range R, k is a calibration factor, and β and σ are the atmospheric backscattering cross sections and the extinction coefficients, respectively, in the planes of polarization orthogonal ($\perp$) and parallel ($\parallel$) to that of the laser. If $\sigma_{\parallel}\cong\sigma_{\perp}$, the lidar depolarization ratio is expressed as [28]

$$\delta(R)=k_{\parallel}N_{\perp}(R)/k_{\perp}N_{\parallel}(R)=k_0\,\beta_{\perp}(R)/\beta_{\parallel}(R), \tag{4}$$

where, k_0 is a calibration factor.

In the CDL, the quality of the raw data is usually estimated by the CNR, which can be calculated conveniently from the power spectrum in each range bin. According to the theory of the CDL, the CNR at different polarization states may be expressed as

$$CNR_{\perp}(R)=\frac{\eta_a\eta_{ox}}{F_h}\frac{T^2\beta_{\perp}(R)}{h\nu B}\frac{E_0c}{2}\frac{A_0}{R^2}, \tag{5}$$

$$CNR_{\parallel}(R)=\frac{\eta_a\eta_{ox}}{F_h}\frac{T^2\beta_{\parallel}(R)}{h\nu B}\frac{E_0c}{2}\frac{A_{r0}}{R^2}, \tag{6}$$

where, η_a is the antenna efficiency, η_{ox} is the optical efficiency, F_h is the noise factor, B is the bandwidth of detector, T is the atmospheric transmittance, which is assumed to be

Optics EXPRESS

$$T = \exp\left[-\int_0^R \sigma_{\parallel}(r) + \sigma_{\perp}(r)\,dr\right] \approx \exp\left[-2\int_0^R \sigma_{\parallel}(r)\,dr\right]. \quad (7)$$

Using Eqs. (2)-(6), we obtain the following relation between the lidar depolarization ratio and the CNRs at two orthogonal states

$$\delta(R) = k_0\, CNR_{\perp}(R)/CNR_{\parallel}(R). \quad (8)$$

3. Experiments

Three sets of experiments are presented in this section. First, the capability of simultaneous detection of the wind velocity and the ADR is demonstrated. Second, to test the detectivity with a radial velocity error of 0.5 m/s, the lidar was pointed horizontally for wind detection only. Finally, a continuous detection of wind velocity in the atmospheric boundary layer was performed to show the stability of the system.

3.1 Depolarization and wind velocity detection

Wind velocity and ADR were detected simultaneously at Hefei (31.83 °N, 117.25 °E) in Anhui province, China. The location is 29.8 m above the sea level. In the experiment, the collimated laser beam is pointed north horizontally. Figure 4 shows the radial wind profiles retrieved from backscattering at the two orthogonal polarization states over half an hour, starting at 23:50 on Mar. 17, 2017. The inset in Fig. 4 is the histogram of velocity difference between S and P state. The statistical size is 19022 between the detection range from 0.3 km to1.8 km. One can see that, the spatial and temporal eddy structures from each polarized state are in good agreement. The mean and standard deviation of the velocity difference are –0.02 m/s and 0.83 m/s, respectively, demonstrating the accuracy of the system. The temporal and radial range resolution of the detection is 2 s and 60 m, respectively.

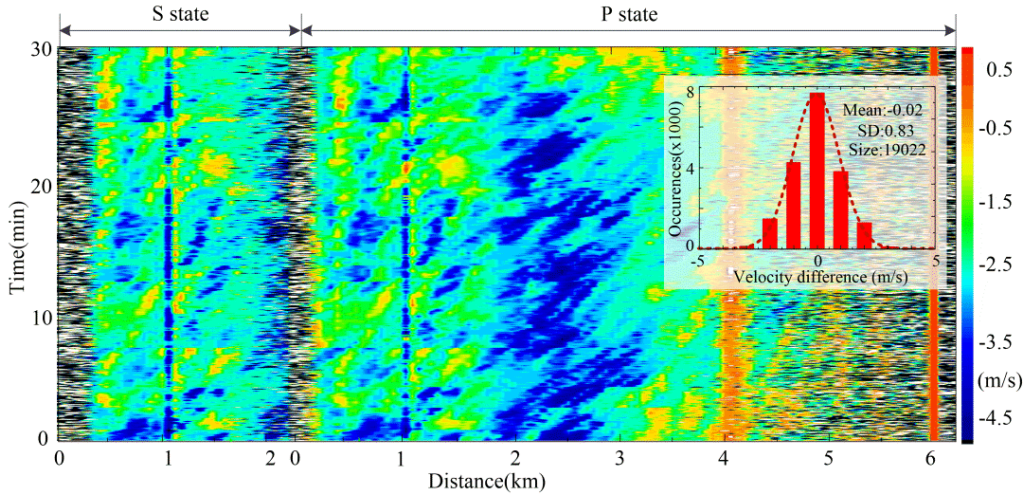

Fig. 4. Wind velocity retrieved from both S and P states backscattering by single balanced detector. The black points represent invalid data points where the carrier to noise ratio (CNR) is low. The inset histogram shows the velocity difference between S state and P state. The temporal and radial range resolution is 2 s and 60 m, respectively, starting at 23:50 on Mar. 17, 2017

In this work, although the ADR is low, as calculated later, the backscattering at S state can be used to retrieve wind velocity as far as 2.1 km. In fact, the power spectrum at both S and P states can be added to reduce the uncertainty of the wind velocity. This feature will be of great importance in some extreme weather conditions, such as a dust storm [29], heavy air

Optics EXPRESS

pollution or boundary layer near the sea surface [30], when the ADR can approach 0.5 [31, 32]. In such conditions, the backscattering at the S state can enhance the CNR and improve the uncertainty of the wind velocity substantially. Figure 5(a) and 5(b) shows the CNR detected at both polarization states. The temporal and spatial resolution is 2 s and 60 m, respectively.

In the range from 0.3 km to 2 km, the CNR of backscattering at S state is between −26 dB and −32 dB, compared to that between −19 dB and −26 dB at the P state. Using Eq. (8), the ADR distribution in this range is calculated as shown as Fig. 5(c). The average ADR is about 0.23 and the maximum ADR is 0.3, a high value of ADR indicates the presence of non-spherical particles in the aerosols, which may due to the heavy air pollution during the experiment. In the distance from 1.5 km to 2 km, the ADR bursts up to 0.3 sometimes. It turns out that the road in the range is under construction. Some of the variability in this range versus time field may due to the small CNR and the fluctuation of the laser power. The temporal and distance resolutions of this detection are 10 s and 60 m, respectively.

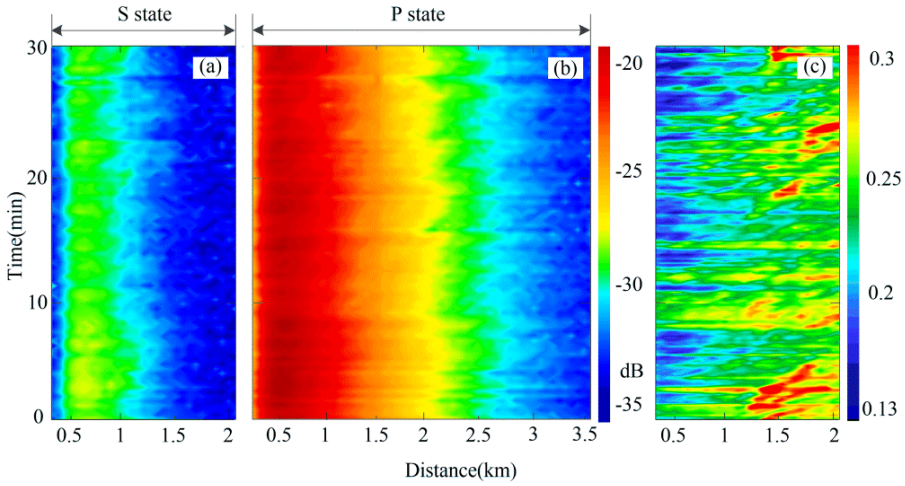

Fig. 5. (a). The CNR distribution of S states. The temporal and spatial resolution is 2 s and 60 m, respectively. Figure 5(b). The CNR distribution of P states. The temporal and spatial resolution is 2 s and 60 m, respectively. Figure 5(c). The distribution of ADR measured by the polarization CDL. The temporal and spatial resolution is 10 s and 60 m, respectively.

3.2 Long range wind velocity detection

In some cases, only wind velocity is needed [33–35], the CDL can be switched from polarization mode to traditional mode by connecting point A to point B directly in Fig. 1(a). By removing the TDM module, the power of backscattering at the parallel state will be preserved without additional attenuations of the PBS, PMF, and OS. Thus, the detectivity will be improved if the ADR is low. Figure 6 shows the detection result of radial wind velocity over half an hour, starting at 00:30 on Mar. 18, 2017. Typical measured CNR and power spectra at different distances are also plotted. The temporal and radial range resolution is 2 s and 60 m, respectively.

Since the telescope is still pointed horizontally to the north, the laser beam is blocked by the same tall building 6060 m away. The wind slows down due to a number of tall apartment buildings at distance of 4.2 km. An interesting phenomenon is that, the radial wind velocity always shows acceleration at distance of 1.1 km. It turn out that, the laser beam goes through the gap between two tall buildings (International Financial Center, Anhui). During the experiment, as the wind blows from the south direction, the flow is restricted and accelerated in the gap between the two buildings.

Optics EXPRESS

In this polarization CDL, an unbiased MLDSP estimator was used, the velocity variance of any unbiased estimator should be higher than a particular bound known as the Cramer-Rao lower bound (CRLB). According to Levin's estimation with an assumption of a Gaussian laser pulse, the CRLB of a CDL velocity variance can be written as [36–38]:

$$v_{CRLB}^2 = \frac{\lambda F_s}{2}\frac{\Delta\omega_n^2}{NM}\{\int_{-\infty}^{\infty}\frac{(\frac{f}{\Delta\omega_n})^2}{[1+\frac{CNR}{\sqrt{2\pi}\Delta\omega_n}\exp(-\frac{f^2}{2\Delta\omega_n^2})]^2}df\}^{-1}, \quad (9)$$

where F_s is the sampling rate, $\Delta\omega_n = \Delta\omega / F_s$ is the normalized Gaussian spectrum width, N is the number of the accumulated laser pulses, M is the number of samples in each range bin, and f is the RF frequency of the power spectrum. For a well-designed CDL, suppose the bandwidth of the Gaussian spectra in each range bin is known, the velocity variance only depends on CNR and N.

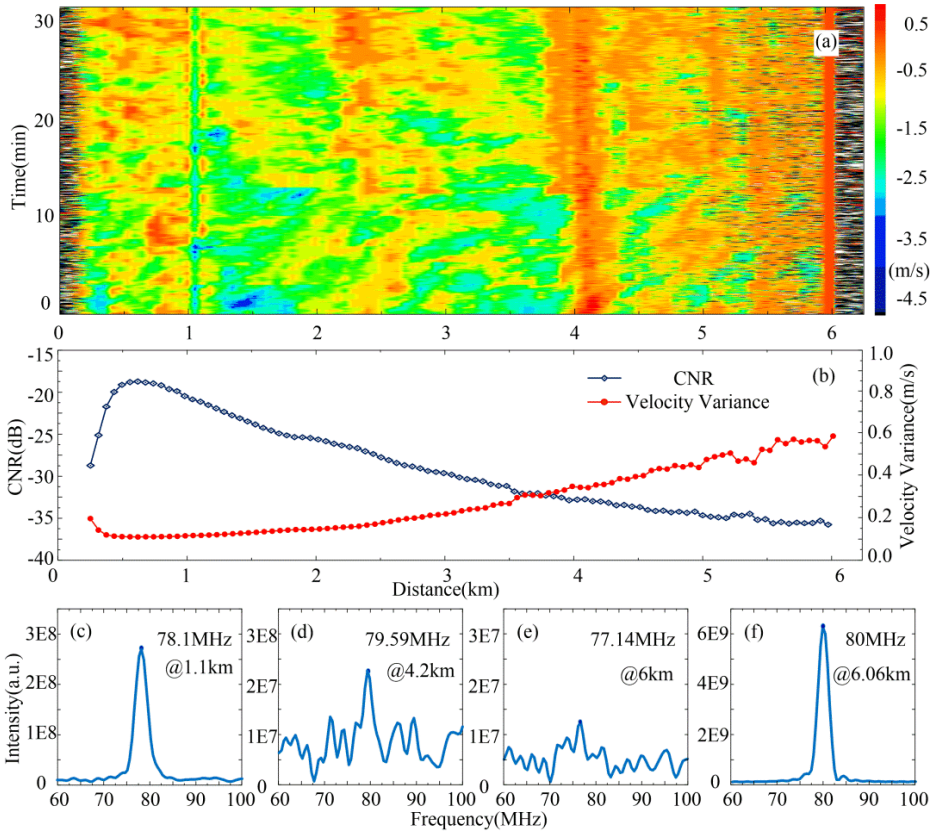

Fig. 6. (a). The horizontal radial wind velocity measured by polarization CDL working in traditional mode. Figure 6(b). The measured CNR and calculated velocity variance distribution. Figure 6(c)-6(f). Corresponding power spectrum at 1.1 km, 4.2 km, 6 km and 6.06 km. The temporal and radial range resolution is 2 s and 60 m, respectively, starting at 00:30 on Mar. 18, 2017

Figure 6(b) shows the measured CNR and corresponding velocity variance with an accumulation of 31250 pulses (2 s). The CNR is between −17 dB to −36 dB from 300 m to 6000 m. Figure 6(c)-6(f) show the power spectra at 1.1 km, 4.2 km, 6 km and 6.06 km. As shown in Fig. 5(c)-5(e), the power spectra at different distances are plotted. The peak power

Optics EXPRESS

intensity decreases as the distance increases. However, as shown in Fig. 6(f), peak power intensity of non-cooperative hard target at 6.06 km is about two orders higher than that of aerosol backscattering at 6 km.

3.3 Continuous observation of vertical wind profiles

In order to demonstrated the stability of the system, a 26-hour vertical wind profiles observation was carried out from 18:00 on Apr. 13 to 20:00 on Apr. 14 in 2017. Two CDLs were used. The laser beams were pointed at two orthogonal azimuths, north and west, with a zenith angle of 30°. The orthogonal meridional and zonal wind velocity are measured and used to compute wind profiles. After two rainy days, the ADR is low. So the CDL was operated in the traditional mode. The horizontal visibility was recorded by a Vaisala PWD-50 simultaneously, as shown in Fig. 7.

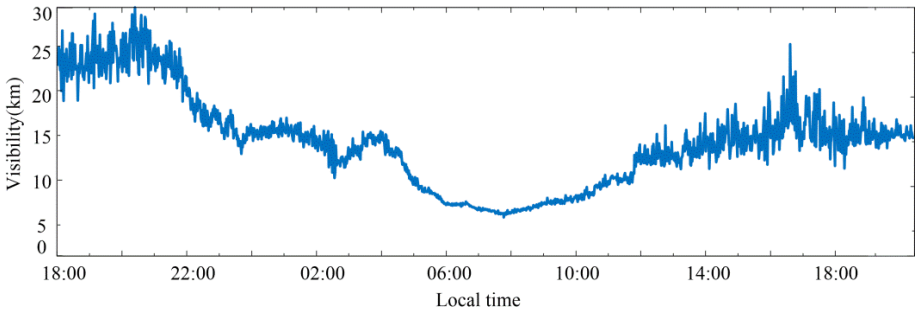

Fig. 7. The visibility recorded by a Vaisala PWD-50 from 18:00 on Apr. 13 to 20:00 on Apr. 14 in 2017.

Figure 8(a)-8(b) show the meridional wind velocity and signal CNR. Figure 8(c)-8(d) show the wind velocity and zonal signal CNR. The discontinuous in Fig. 8(b) is due to the fluctuation of the laser power. With an assumption of horizontally homogeneous and negligible vertical component of wind, the wind direction θ is computed by using the following equations:

$$\theta = \begin{cases} 180\text{-}|\arctan(V_E/V_N)| & \text{if } V_N > 0 \,\&\, V_E > 0 \\ |\arctan(V_E/V_N)| & \text{if } V_N < 0 \,\&\, V_E > 0 \\ 180\text{+}|\arctan(V_E/V_N)| & \text{if } V_N > 0 \,\&\, V_E < 0 \\ 360\text{-}|\arctan(V_E/V_N)| & \text{if } V_N < 0 \,\&\, V_E < 0 \end{cases}, \tag{10}$$

where V_N and V_E is the meridional and zonal wind velocity, respectively. Here, the wind direction is defined as the clockwise angle with respect to the north direction. The magnitude of the wind velocity is

$$V = (V_N^2 + V_E^2)^{1/2}. \tag{11}$$

The temporal and distance resolution of this detection is set to be 60 s and 60 m, respectively. Due to the low aerosol concentration in the atmospheric boundary layer, the maximum detection altitude is set to 3 km. The horizontal wind speed and direction are shown in Fig. 8(e) and Fig. 8(f), respectively. The dynamic evolution and structure of the wind velocity can be seen clearly.

Optics EXPRESS

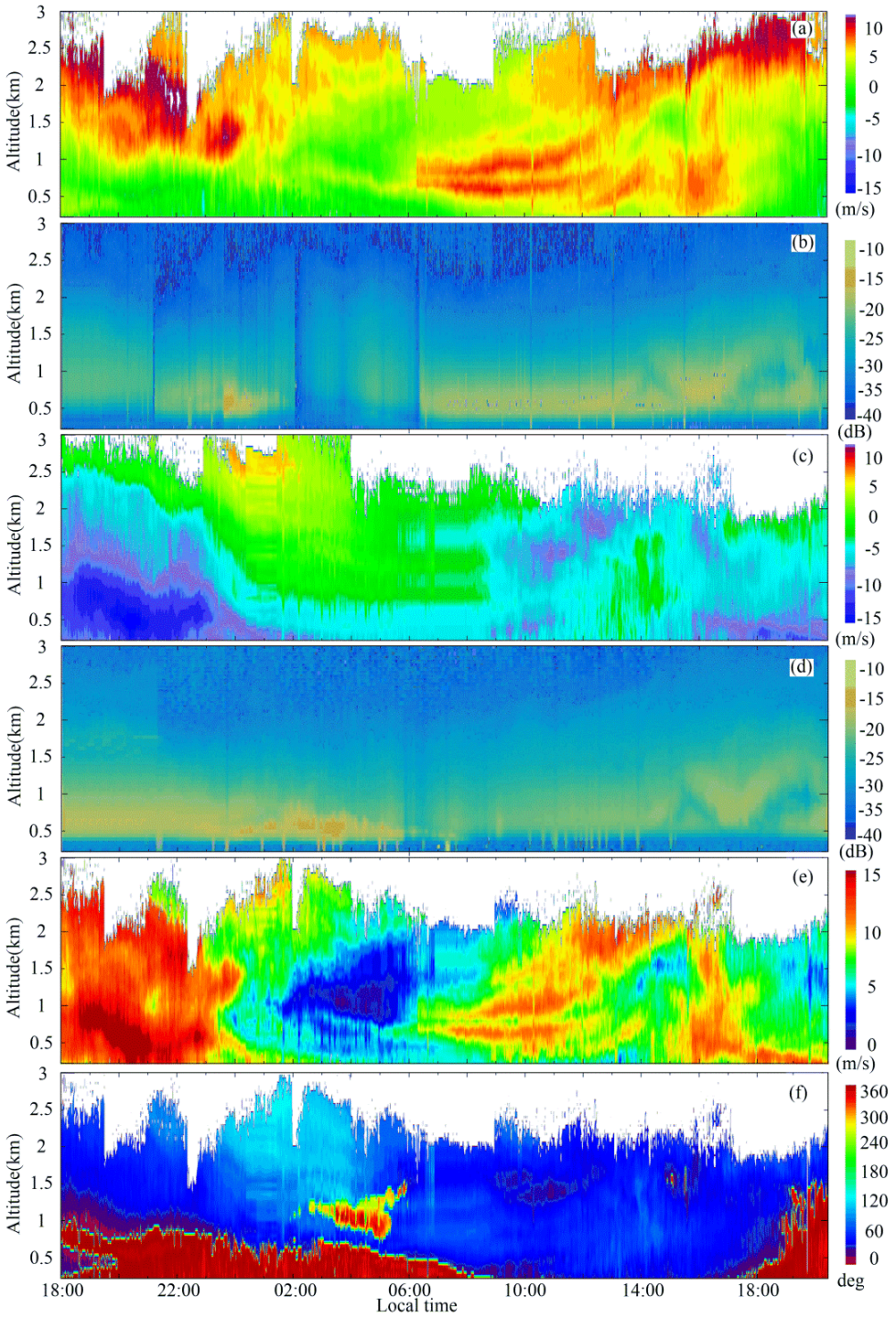

Fig. 8. (a). The meridional wind velocity, an updraft can be seen in the daytime. Figure 8(b). CNR distribution of the meridional signal. Figure 8(c). The zonal wind velocity, a zero radial wind layer is declining during the night. Figure 8(d). CNR distribution of the zonal signal. Figure 8(e). Horizontal wind speed. Figure 8(f). Horizontal wind direction. The temporal and spatial resolution is 60 s and 60 m, respectively. The observation is from18:00 on Apr. 13 to 20:00 on Apr. 14 in 2017.

Optics EXPRESS

4. Conclusion

A polarization coherent Doppler lidar for simultaneous detection of the wind velocity and the atmospheric depolarization ratio was demonstrated. Thanks to the low attenuation in fiber in the optical communication band, the time-division multiplexing technique was applied to simplify the optical layout, making the system stable and robust. Backscattering components at parallel and perpendicular polarization states were measured by using a single balanced detector. Thus systematic error induced by the non-uniform response of different detectors in traditional lidars was moved out. The experiments proved that: on one hand, the perpendicular components of the backscattering can be used to detect the atmospheric depolarization ratio; on the other hand, it can enhance the carrier to noise ratio in wind detection. With a radial velocity error of 0.5 m/s, the detection range of the lidar in the traditional mode can approach 6 km, when the temporal and spatial resolution was set to 2 s and 60 m, respectively. During a continuous observation period of 26 hours, the system obtained vertical variability of the wind.

Acknowledgments

The authors are grateful to the anonymous reviewers for their constructive comments.

222.195.79.199 {ts '2017-08-17 02:55:42'}